

https://dspace.org/

Phonondrag in a graphite channel buried in diamond

S. Salami; R. Debord; V.M. Giordano; R. Fulcrand; Nyiku Mahonisi ...

https://hdl.handle.net/10539/40487
WOS

Downloaded from a DSpace repository. https://dspace.org/

Solid State Sciences 151 (2024) 107494

Contents lists available at ScienceDirect

Solid State Sciences

journal homepage: www.elsevier.com/locate/ssscie

Phonon-drag in a graphite channel buried in diamond

S. Salami [a], R. Debord [a], V.M. Giordano [a], R. Fulcrand [a], N. Mahonisi [b,c], Z. Mthwesi [b], N. Blanchard [a], A. Every [b], S. Vignoli [a], C. Adessi [a], S.R. Naidoo [b,c,d,**], S. Pailhès [a,*]

[a] CNRS, University of Lyon, Université Claude Bernard Lyon 1, Institut Lumière Matière, F-69622, Villeurbanne, France
[b] School of Physics, University of Witwatersrand, Private Bag 3, Johannesburg, 2050, South Africa
[c] DSI-NRF Centre of Excellence in Strong Materials, University of Witwatersrand, Private Bag 3, Johannesburg, 2050, South Africa
[d] Materials Physics Research Institute (MPRI), School of Physics, University of Witwatersrand, Private Bag 3, Johannesburg, 2050, South Africa

ARTICLE INFO

Keywords:
Implanted diamond
Buried channel
Seebeck
Electron-phonon interaction

ABSTRACT

While the phonon-drag effect can induce large Seebeck coefficients, it is associated with large mean free path phonons present in the vicinity of the maximum in temperature of the lattice thermal conductivity. In this paper, we initiate a new route by searching for the mutual drag between the electron and phonon-drag gases at the interface between two different media. In that respect, the temperature studies of the conductance and Seebeck coefficient of a model system consisting of an electrically conductive graphitic channel buried beneath the surface of a diamond crystal are shown. The observed behaviour is very similar to that of graphite, with a typical negative peak associated with the phonon-drag effect. Interestingly, this phonon-drag peak of the buried graphitic channel appears at a significantly higher temperature than that in pure graphite.

1. Introduction

Ion implantation is a useful tool in the semiconductor industry used to create p-type and n-type preselected regions in a semiconductor [1,2]. In most semi-conducting materials like Si and Ge, the displaced atoms in the collision cascade return to their lattice atomic positions because the vacancies and interstitials have similar activation energies for their mobility. Subsequent annealing in such materials recovers the original lattice structure by solid-phase epitaxial regrowth [3]. Similar implantation processes have been used to dope diamond. The challenges are that in diamond, the sp^3 bonds that are broken during implantation are more likely to assume an sp^2 configuration. Because the interstitials are mobile at lower temperatures while the vacancies only become mobile above 500 °C it becomes unlikely to recover the diamond structure after annealing if the radiation damage exceeds a critical level [4–8]. In the energy regime for the implantation used in this study, solid-phase epitaxial regrowth of diamond is not observed at any annealing temperature at ambient pressure. Similar behavior has been observed in studies using MeV ion implantation [9]. This effectively means that one can use ion implantation to transform diamond to an amorphous/-graphitic carbon state. By a judicious choice of energy and fluence, one can create buried amorphous channels below the diamond surface. When the level of damage density surpasses a critical point, often referred to as the "graphitization threshold", and subjecting the damaged structure to high-temperature thermal annealing, the amorphous/graphitic volume displays ohmic conductivity. Instances of such behavior can be observed in the case of buried conductive channels formed through MeV ion implantations, as discussed in Refs. [5,10]. Conversely, when the damage density falls short of the critical threshold and/or the sample is not subjected to high-temperature annealing, the conduction mechanism within the resulting amorphized layers can be described using more complex models based on variable range hopping. This was initially explored by Hauser et al. [11,12] and further investigated by Prins [13,14]. In this scenario, unlike the former case where conductivity is clearly attributed to band-like charge transport within a graphite-like medium, models that are more intricate must be employed. Detailed works by Kalish et al. [15–17] and other research groups [18–20] have delved into this, extracting various characteristic energies for hopping transitions from the temperature-dependent resistivity data.

The mutual drag between electrons and phonons under the effect of a temperature gradient or a current results from a coupling between the two Boltzmann transport equations for electrons and phonons due to electron-phonon coupling. It amplifies the Seebeck and Peltier coefficients and this is generally observed at low temperatures when the

* Corresponding author.
** Corresponding author. School of Physics, University of Witwatersrand, Private Bag 3, Johannesburg, 2050, South Africa.
E-mail addresses: mervin.naidoo@wits.ac.za (S.R. Naidoo), stephane.pailhes@univ-lyon1.fr (S. Pailhès).

https://doi.org/10.1016/j.solidstatesciences.2024.107494
Received 15 November 2023; Received in revised form 6 February 2024; Accepted 23 February 2024
Available online 9 March 2024
1293-2558/© 2024 The Authors. Published by Elsevier Masson SAS. This is an open access article under the CC BY-NC license (http://creativecommons.org/licenses/by-nc/4.0/).

phonon mean free paths are large, *i.e.* in the vicinity of the maximum in temperature of the lattice thermal conductivity. Electrical conducting channels embedded in an insulating diamond matrix provide a model system for re-exploring the phonon-drag effect for thermoelectricity, in conjunction with recent theoretical [21–23] and experimental [24–27] works showing the possibility of amplifying the thermoelectric power factor using the phonon-drag effect in the Seebeck while maintaining low thermal conduction. Indeed, it allows to explore the effects of electron-phonon interaction at interfaces, and in particular the existence of a mutual drag between the electron and phonon gases on either side of the interface when a temperature gradient is applied. An example of such substrate effect on the position and amplitude of the phonon-drag peak was reported in thin films of Bi_2Te_3 [28]. As far as we can ascertain from published literature, the behaviour of the Seebeck coefficient (S) of a conducting buried channel at low temperatures has not been studied.

In this paper, we report measurements of the Seebeck coefficient and resistivity in a 145 nm thick channel buried 200 nm below the surface of a diamond crystal. The room temperature conductance measured in the sample is in the range of graphite and its temperature dependance reflects the presence of extended conductive regions. The Seebeck coefficient shows a behavior very similar to graphite, with a negative peak at low temperatures associated with a phonon-drag effect at a significantly higher temperature than that in pure graphite.

2. Experimental

2.1. Implantation and annealing

A CVD single crystal diamond with polished faces oriented in {100} and of dimension $3 \times 3 \times 0.3$ mm^3 polished on one side was purchased from Element Six. The implantation was done at iThemba LABS, Gauteng, South Africa with a Varian 200-A2F ion implanter equipped with an experimental end-station. The implantation was done on the polished face with He ions at an energy of 80 keV to a fluence of 3×10^{16} ions.cm^{-2}. The choice of He in this study was used because it is chemically inert and will not induce any chemical changes in the implanted volume and hence all changes can be attributed to the redistribution of the carbon atoms and their chemical bonds in the implanted range. The target was fixed on a target holder inside a vacuum chamber of a typical pressure of $\approx 10^{-6}$ mbar. A scanned beam of current density of $\approx 10^{13}$ ions.s^{-1} was used and the sample was oriented at 5° to the direction of the beam. The sample was cooled to liquid nitrogen temperature before the implantation and kept at liquid nitrogen prior to annealing in a preheated crucible at 1200 °C in an argon atmosphere. The full annealing process for cold implantation rapid annealing (CIRA) is described in Ref. [4]. After annealing, the diamond was cleaned by boiling in an oxidizing acid solution for about 20 min and rinsed in deionized water [29]. The sample was implanted over the entire surface but later mechanically filed along the edges. This was done to ensure that the edges, which are conductive as supplied by Element Six, do not influence the transport measurements done through the surface. By filing the edges we were able to isolate the implanted surface by removing the conductive layer which is created during the laser kerf of the supplier.

2.2. SRIM

To determine the position of the amorphous region created due to the chosen implantation conditions, the simulated damage as predicted by SRIM (Stopping range of ions in matter) [30] has been determined to be where the simulated damage density exceeds a value which is between 1 and 9×10^{22} vac.cm^{-3} [9,31–34]. SRIM is a Monte Carlo simulation used to predict two aspects of ion implantation: the maximum range reached by the implanted ions and the resulting damage profile within the target material. Any region within the simulated damage density ($1 - 9 \times 10^{22}$ vac.cm^{-3}) will transform into amorphous carbon after annealing above 600 °C [31,34–36]. For high enough fluences implanted at ambient pressure and temperatures below 500 °C the transformation of diamond to amorphous carbon takes place during the implantation process. The diamond implanted at these high fluences at the conditions described earlier becomes black after implantation. Fig. 1a illustrates an example of a simulated damage profile, quantified in terms of vacancies/cm^3, as a function of depth. This profile was generated through a SRIM simulation for an implantation of He ions with an energy of 80 keV to a fluence of 3×10^{16} vac.cm^{-2} into diamond (C 3.515 g cm^{-3}) at a displacement energy of 50 eV. In this simulation, the full damage cascades calculation was used to generate the damage profile.

In order to estimate the width of the amorphous region after implantation and annealing, a bright field Transmission Electron Microscopy (TEM) image was obtained from the implanted sample (Fig. 1b). A lamella of the implanted volume from the diamond surface to a depth far beyond the implantation range was extracted from the sample using Focused Ion Beam (FIB) milling with a FIB Zeiss NVision 40 at Lyon Saint Etienne Microscopy Consortium (CLYM). The lamella was thinned to be electron transparent and a Precision Ion Polishing System (PIPS) was used to clean the lamella before imaging. The cross-sectional TEM images were recorded at 200 kV with a JEOL 2100 microscope with a LaB6 electron source located at the Institute of Light and Matter (ILM). The contrast seen in Fig. 1b is dominated by increased elastic scattering of electrons out of the direct transmitted beam in the regions with long range order. The absence of Bragg diffraction in the disordered region means that more electrons passing through this region remain undeviated, therefore the disordered region appears brighter in the bright field image; where region B corresponds to non-crystalline material while regions A and C correspond to crystalline diamond [9,37]. The depth established from the TEM ($\approxeq$ 200 nm) was correlated with the corresponding damage density in our simulated damage profile (Fig. 1a). This density corresponds to the threshold of permanent damage and was found to be $\approxeq 6 \times 10^{22}$ vac.cm^{-3} for these implantation and annealing conditions. Using this threshold, the simulation shows that the damage starts at a depth of $\approxeq$ 200 nm below the surface of the diamond and extends to a depth of $\approxeq 305 - 310$ nm leaving us with a damage region that is $\approxeq$ 100 nm thick. However, from the TEM image after 1200 °C annealing (Fig. 1b), it is observed that the width of the damage is about $\approxeq 140 - 150$ nm. There is therefore around $40 - 50$ nm of amorphous carbon in the sample that is not accounted for in the TRIM simulation. The implantation and annealing process creates a less denser material which causes swelling of the implanted volume [7,9,38–43]. The additional 50 nm observed in the TEM images is associated with the swelling of the amorphous region.

2.3. Resistance and Seebeck measurements

Metallic electrodes were implemented to ensure ohmic contact with the buried region for the study of its electric and thermoelectric properties. The implemented method to create the electrodes on this sample included milling holes in the diamond using FIB. The milled holes (four small squares appearing inside the pads in Fig. 2a) were 100×100 μm^2 and the depth extended to an average of 600 nm which was beyond the extent of the implanted range. The holes were then filled with a metal stacking of 350 nm of Titanium (Ti), 50 nm of Chromium (Cr), and finally 150 nm of Gold (Au). The metal desposition was followed by an annealing at 450 °C [44–46]. The implemented electrodes are shown in Fig. 2a with the squares inside the pads showing where the FIB milled holes are located (highligheted in Fig. 2a with the red dashed squares).

In-plane impedance measurements were carried out between the two electrodes and from the surface, with connections placed at a spacing identical to that between the electrodes. In this geometry (2-wire electrical measurement), the measurement is mostly dominated by the contact resistance. From the measurement, we can see that the real part of the impedance (Re(Z)) is constant as function of frequency reflecting

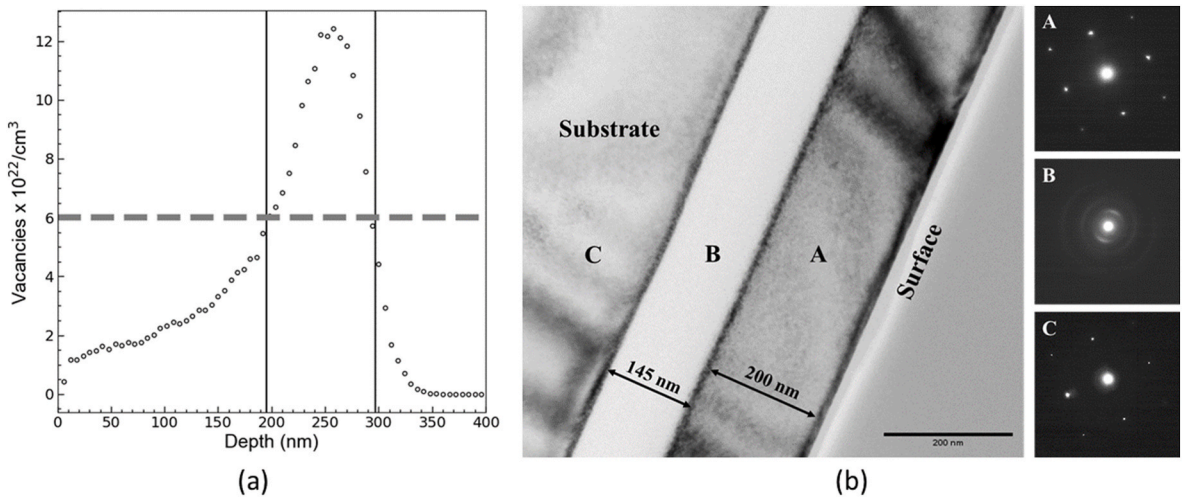


Fig. 1. (a) Damage profile (vacancies/cm^3 as a function of depth) predicted by the SRIM. The corresponding width of the amorphous channel (≅ 100 nm) in the implanted and annealed region is predicted to be below the surface of the diamond from a depth of ≅ 200 nm (left vertical line) to a depth of ≅ 300 nm (right vertical line) for the chosen threshold of 6×10^{22} vac.cm^{-3} lying within the $1 - 9 \times 10^{22}$ vac.cm^{-3} range. (b) A bright-field TEM micrograph of the sample (annealed at 1200 °C revealing the buried channel (disordered carbon/amorphous region) of a thickness of 145 nm embedded in a crystalline diamond at a depth of approximately 200 nm. Three insets display selected area electron diffraction (SAED) patterns for regions A and C, illustrating the diamond structure in the same orientation. Two bright arcs close to the center of the SAED inset for region B indicate partial alignment of basal planes from bent (002) graphitic structures [37].

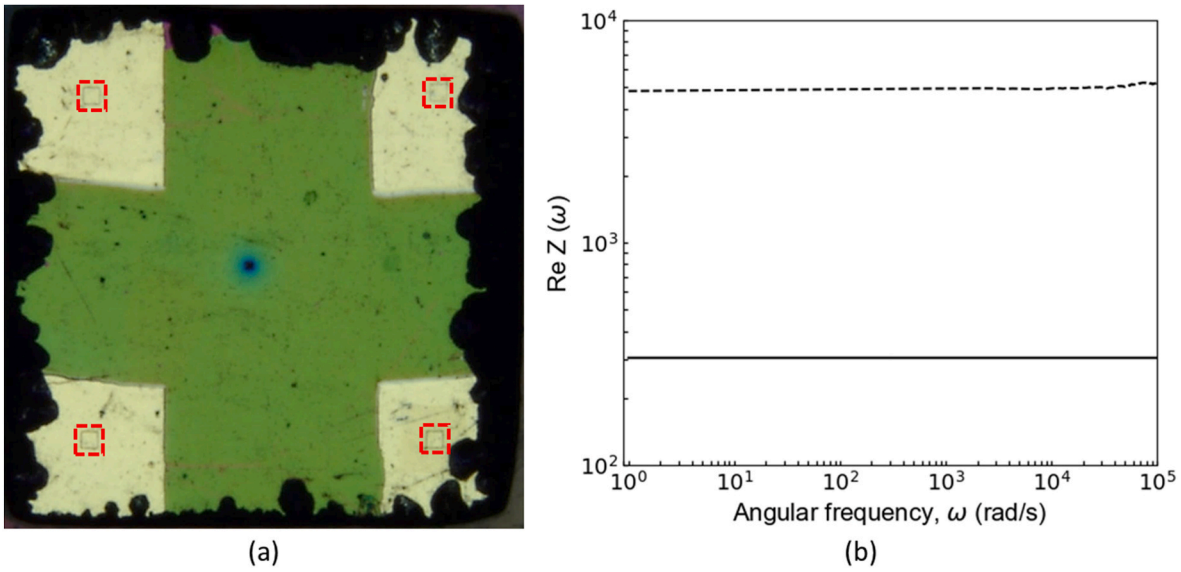


Fig. 2. (a) Optical image of the sample with metallic pads, the small squares inside the pads are where the FIB milled holes are located (b) Comparison in impedance measurements Re(Z) in the broad frequency range 1Hz – 1 MHz between the electrodes (black solid line) and the surface (black dashed line).

the ohmic behaviour. The difference in (Re(Z)) between the surface and the electrode is shown in (Fig. 2b). The values of Re(Z) at low frequencies correspond to the DC part of the resistance, where we can see that the one measured through the electrodes is about one order of magnitude smaller than that measured from the surface. The difference between the Re(Z) measured from the surface and that measured through the electrodes proves that the buried electrodes ensure a successful electric connection to the buried channel. A noteworthy observation is that although the resistance measured from the surface is higher than that measured through the electrodes, it is still much lower than that of diamond which implies the presence of high resistance pathways connecting the buried region to the surface inducing the measurement of a lower impedance than that in diamond but higher than that in the channel.

Low-temperature measurements of resistivity and the Seebeck coefficient were conducted in a high vacuum environment (pressure ≈ 10^{-7} mbar) using a custom-made apparatus at the ILM. The design of this apparatus was inspired by the configuration described in Ref. [47], with a resolution of $< 1\mu$V.K^{-1}. The setup featured a helium-closed-cycle 4K Sumitomo cryostat (RDK-101DL) with the sample securely mounted on a circuit attached to the cryostat's cold finger. Additionally, the setup incorporated thermal shielding to protect against radiation. The temperature range at the sample location could be regulated, varying from 8 K to 300 K. Resistance measurements were performed using the delta mode, with both positive and negative current, of the combined Keithley current source (K6220) and nanovoltmeter (K2182A). For each temperature step, an I–V curve was measured by varying the current within the [0:100]μA range, from which the resistance was extracted (raw data are presented in Fig. 3a). It's noteworthy that the I–V curves remained linear within this current range across the entire temperature range. The Seebeck coefficients (S) were determined using the differential method.

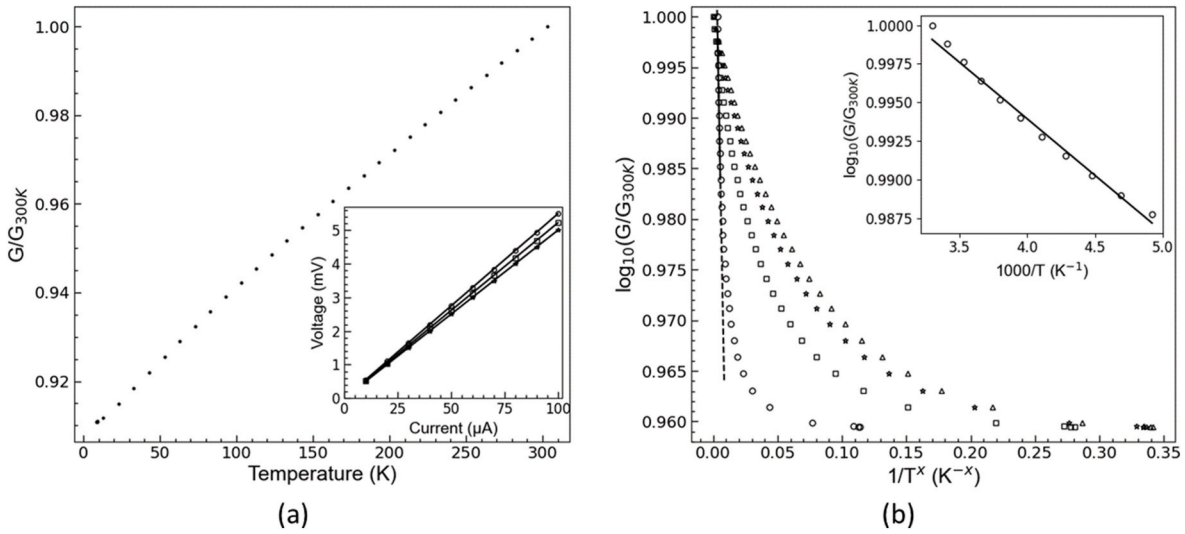


Fig. 3. (a) Temperature dependence of the normalized conductance G/G_{300K}, the inset shows Delta I–V measurements (points) at different temperatures and the linear fits (solid lines): (∘) for 10 K, (□) for 150 K, and (⋆) for 300 K. (b) The $\log_{10}$ plot of G/G_{300K} vs $1/T^x$ with x = 1 (∘), x = 1/2 (□), x = 1/3 (⋆) and x = 1/4 (△) from the left to the right. To simplify reading, the points have been reduced to the same abscissa value. The inset figure is the linear fit in a small temperature range of $\log_{10}(G/G_{300K})$ vs 1000/T.

3. Results and discussions

The temperature-dependent conductance, normalized to its value at room temperature, is illustrated in Fig. 3a. The room temperature conductance measured is 0.02 S and the corresponding sample conductivity calculated using a thickness and its uncertainties (see above) of 145 ± 20 nm is determined to be approximately $\sigma_{300K} = 300 \pm 41$ S cm^{-1} (equivalent to a resistivity of $\rho_{300K} = (3.3 \pm 0.4) \times 10^{-3}$ Ω cm). This value is comparable to values known in ion implanted diamond beyond the graphitization threshold [5,48,49]. Going down in temperature, the conductance smoothly decreases and tends toward a finite residual value at the lowest probed temperature (8 K), indicating that conduction in the buried channel is on the metallic side of the metal-insulator transition. We attempted to analyze its temperature dependence using conventional forms of temperature dependence for hopping conductivity, plotting the logarithm of the ratio $G(T)/G_{300K}$ versus $1/T$, $1/T^{1/2}$, $1/T^{1/3}$, and $1/T^{1/4}$. No linear regime was clearly observed over a significant temperature range among all the different laws. This confirms the presence of extended conductive regions. The best linearity is obtained with the $1/T$ law at high temperatures (see the inset and the solid line in Fig. 3b). When fitting within this range, an activation energy of approximately 1.45 meV (equivalent to 17 K) is obtained.

The temperature dependence of the Seebeck coefficient in the buried channel is shown in Fig. 4. It starts at approximately −5 μV K^{-1} at 300 K. The negative sign of the Seebeck at room temperature, where the phonon-drag contribution is assumed to be negligible, agrees with measurements reported in graphite. From galvanometric [50] and thermoelectric measurements [51–55], the negative sign of the Seebeck in graphite was interpreted as a higher mobility of electrons compared to holes. The Seebeck coefficient then remains nearly constant down to about 150 K. Upon further cooling, it exhibits a negative peak of about −7.5 μV K^{-1} at around 65 K and then tends towards zero as the temperature approaches zero, eventually reaching a positive value of nearly +2 μV K^{-1} at approximately 13 K. The overall temperature dependence closely resembles that measured in graphite, where the negative peak in the Seebeck coefficient at low temperatures is associated with the phonon-drag effect. However, it's worth noting that the peak measured in our sample is observed at higher temperatures (65 K) compared to that seen in graphite (20 − 45 K) [51–54] and is of lower amplitude. In Fig. 4, the colored rectangle highlights the temperature range of the peak temperatures of the Seebeck coefficient (indicated by vertical bars on the x-axis) extracted from Refs. [51–54]. The amplitude of the Seebeck peak reported in the literature varies between −4 and −37 μV K^{-1} [51–54]. The graph shows that the peak maximum of the Seebeck coefficient in our sample occurs at approximately 20–25 K (well beyond the experimental uncertainties) above the peak maximum observed in graphite.

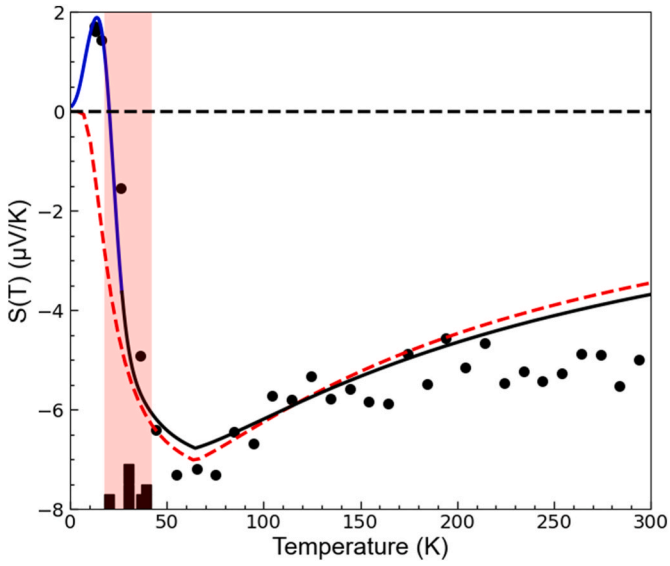


Fig. 4. Graph showing the measured Seebeck coefficient (S) and its corresponding fit. The black dots correspond to the experimental data measured from the sample. The red dashed line corresponds to the fit from the model. The solid lines corresponds to the model with the addition of the gaussian fit for the positive Seebeck values where the blue solid line shows the phenomenological gaussian fit and the black solid line shows the model fit with the Gaussian. The colored rectangle highlights the temperature range of the peak temperatures of the Seebeck coefficient (indicated by vertical bars on the x-axis) extracted from references [51–53].

Given that the sample exhibits an electric resistivity falling within the range typically associated with graphite [5,49] and demonstrates similar Seebeck tendencies, we endeavored to apply a toy model

developed by Ref. [51] in 1970 to examine the effects of "phonon-drag" in graphite. In their work, the authors evaluated the additional phonon-drag component in the Seebeck coefficient by calculating the electron-phonon coupling between in-plane acoustic phonons and in-plane electronic states in the vicinity of the Fermi level. They considered only the acoustic phonons whose wave vectors, $q = \hbar\omega/v_s$ (where $\hbar\omega$ is the phonon energy and v_s is the average sound velocity) connect the Fermi surface, also referred to as Kohn phonons. The wave-vector amplitude of these Kohn (K) phonons satisfies the relation $q_K = 2k_f$, where k_f is the Fermi wave vector. This corresponds to a characteristic phonon energy ($\hbar\omega_K$) and temperature (T_K) given by $k_B T_K = \hbar\omega_K = 2v_s k_f$. Assuming that electron-phonon scattering is predominantly dominated by the scattering with the Kohn phonons, they derived an analytical solution for the coupled phonon/electron Boltzmann transport equations within the relaxation time approximation. From this solution, and with assumptions detailed in the paper, they calculated the phonon-drag contribution to the Seebeck coefficient, which can be expressed as:

$$|S_{drag}(T)| \propto C_{ph}(T) \frac{\Gamma(T)}{\Gamma(T) + \frac{1}{\tau_{ph}}} \quad (1)$$

where Γ function quantifies the deviations of the equilibrium phonon/electron statistics from their mutual collisions. This Γ is constant (A) for $T < T_K$ and varies with T_K/T for $T > T_K$. $C_{ph}(T)$ corresponds to the specific heat of the Kohn phonons described by an Einstein-like mode with an energy $\hbar\omega_K$. τ_{ph} is the phonon relaxation time for all collisions other than the electron-phonon scattering. Within the temperature range of T_K, τ_{ph} is assumed to be constant as being dominated by the Casimir like scattering processes. From Eq. (1), it comes that $S_{drag}(T)$ is divided into two segments $C_{ph}(T)$ and the fraction which depends on $\Gamma(T)$. The sum of these two segments has been represented in Fig. 4 (red dashed lines).

The negative peak in $S_{drag}(T)$ results from the intersection of these two segments: starting from the lowest temperatures, its amplitude increases with heating due to the populating of Kohn phonon states, following $C_{ph}(T)$, then decreases following a 1/T law when phonon-phonon scattering processes are thermally activated. Using this expression of $S_{drag}(T)$ and by fixing $\hbar\omega_K$ to a value of 5.6 meV (*i.e.* 1.35 THz) corresponding to T_K = 65 K (temperature of the peak maximum observed on the graph) we fitted the following parameters A and $1/\tau_{ph}$ and obtained the corresponding values: $A = 3 \times 10^8$ and $1/\tau_{ph} = 1.5 \times 10^8\ s^{-1}$. Our values agree with the ones observed in graphite. However, as a result of a higher peak temperature for the Seebeck, our average Kohn phonon energy is higher than the one extracted in Ref. [51]. This is either due to a difference in electronic structure, or it is the result of a broadening of the energy band around the Kohn energy of the phonons that contribute most to the phonon-drag effect. In the latter case, it could be the signature of the contribution of the phonon states of the diamond matrix coating the conduction channel.

Finally, we propose to discuss the deviations observed in Fig. 4 from the simple model (Eq. (1)), which are also observed in graphite. In fact, the structure of the phonon-drag peak in graphite can be much more complex depending on the quality and annealing of the sample [54]. A double phonon-drag peak structure is observed and associated to a two-stage phonon-drag effect [53–55]. On the other hand, the range of positive values in the Seebeck for temperatures below the one corresponding to the huge negative dip has been reported by different authors on graphite [53–56]. This range is ascribed to the purely electronic diffusive component [51]. To take into account the range of positive Seebeck values observed at the lowest temperature measured below T_K, we added a phenomenological term (a gaussian function) to Eq. (1) centered at $T_0 = 17$ K with a width at half the maximum intensity of 7 K. In Fig. 4, the black solid line shows the total fit (Eq. (1) plus the Gaussian term) and, highlighted in blue, is only the Gaussian part while the dashed red lines give only the fit from Eq. (1) discussed before. At higher temperatures (above 200 K), the fit over-estimates the experimental values. This is mainly caused by incorrectly taking into account the temperature dependence of τ_{ph}.

4. Conclusions

In summary, we presented low-temperature measurements of the electrical conductance and the Seebeck coefficient in a graphitic channel buried in a diamond crystal through He ion implantation to a fluence of 3×10^{16} ions.cm^{-2} and annealing at 1200 °C using the CIRA approach. Under these implantation and annealing conditions, the created buried channel has a thickness of 145 nm and is located at about 200 nm below the surface. The room temperature conductivity is in the range of that of graphite. The conductance displays a smooth temperature dependence with a residual value at the lowest temperature, indicative of extended conducting regions, placing the system in the metallic side of the metal-insulator transition. The temperature dependence of the Seebeck coefficient exhibits tendencies similar to those observed in graphite, characterized by a negative maximum at low temperatures attributed to the phonon-drag effect. Notably, our peak appears at a significantly higher temperature than the phonon-drag peak temperatures reported in the literature in graphite. This indicates an increase in the energies of the phonons primarily involved in the drag effect, which is associated either with a difference in the electronic structure of the conduction channel compared to graphite, or with a contribution from the phonons of the diamond matrix in which the channel is embedded.

CRediT authorship contribution statement

S. Salami: Data curation, Formal analysis, Investigation, Writing – original draft, Writing – review & editing. **R. Debord:** Data curation, Formal analysis, Investigation, Methodology. **V.M. Giordano:** Investigation. **R. Fulcrand:** Investigation, Methodology. **N. Mahonisi:** Investigation. **Z. Mthwesi:** Investigation. **N. Blanchard:** Investigation, Methodology. **A. Every:** Investigation. **S. Vignoli:** Investigation. **C. Adessi:** Investigation. **S.R. Naidoo:** Conceptualization, Funding acquisition, Investigation, Methodology, Project administration, Supervision, Validation, Writing – original draft, Writing – review & editing. **S. Pailhès:** Conceptualization, Data curation, Formal analysis, Funding acquisition, Investigation, Methodology, Project administration, Supervision, Validation, Writing – original draft, Writing – review & editing.

Declaration of competing interest

The authors declare the following financial interests/personal relationships which may be considered as potential competing interests:S. Pailhès - S. R. Naidoo reports financial support was provided by Campus France. S. Pailhès - S. R. Naidoo reports financial support was provided by the Centre National de la Recherche Scientique in France CNRS. S. Pailhès - S. R. Naidoo reports financial support was provided by University of the Witwatersrand Johannesburg. If there are other authors, they declare that they have no known competing financial interests or personal relationships that could have appeared to influence the work reported in this paper.

Data availability

Data will be made available on request.

Acknowledgement

This work is part of a Joint Wits-CNRS 2021 PhD programme, project "ETAIN", and was supported by Campus France programPHC PROTEA 2022 - PROJET N° 47785XL (PION), a research program implemented in France by the French Ministry of National Education, Higher Education and Research (MESR) and the French Ministry of Foreign Affairs and

International Development (MEAE) and, in South-Africa, by the South African Department of Science and Innovation. We would like to thank AS Miller for performing the implantations, Solene Brottet (INL) for extracting the lamella and preparing it for TEM imaging. SR Naidoo would like to thank the DSI-NRF Centre of Excellence in Strong Materials and the South African Quantum Technologies Initiative (SA QuTI) for financial support and iThemba LABS (Gauteng) for the use of the Ion Implanter. S. Pailhès would like to thank Transport@ILMTech for the TE measurements and Clement Albin for support on the mechanical service.

References

[1] R. Kalish, Ion-implantation in diamond and diamond films: doping, damage effects and their applications, Appl. Surf. Sci. 117–118 (jun 1997) 558–569.
[2] J.F. Prins, Ion implantation of diamond for electronic applications, Semicond. Sci. Technol. 18 (3) (feb 2003) S27–S33.
[3] J.S. Williams, Solid phase epitaxial regrowth phenomena in silicon, Nucl. Instrum. Methods Phys. Res. 209–210 (may 1983) 219–228.
[4] I. Motochi, B.A. Mathe, S.R. Naidoo, D. Wamwangi, T.E. Derry, Surface brillouin scattering observation of higher order resonances in annealed, ion-implanted CVD diamond, Diam. Relat. Mater. 76 (jun 2017) 171–176.
[5] A.A. Gippius, R.A. Khmelnitskiy, V.A. Dravin, S.D. Tkachenko, Formation and characterization of graphitized layers in ion-implanted diamond, Diam. Relat. Mater. 8 (8–9) (aug 1999) 1631–1634.
[6] J.O. Orwa, K.W. Nugent, D.N. Jamieson, S. Prawer, Raman investigation of damage caused by deep ion implantation in diamond, Phys. Rev. B 62 (9) (sep 2000) 5461–5472.
[7] A.V. Khomich, R.A. Khmelnitskiy, V.A. Dravin, A.A. Gippius, E.V. Zavedeev, I. I. Vlasov, Radiation damage in diamonds subjected to helium implantation, Phys. Solid State 49 (9) (sep 2007) 1661–1665.
[8] I. Motochi, B.A. Mathe, S.R. Naidoo, E. Aradi, Anomalous behaviour of surface brillouin scattering in thin strained cvd diamond, Diam. Relat. Mater. 109 (nov 2020) 108020.
[9] D.P. Hickey, K.S. Jones, R.G. Elliman, Amorphization and graphitization of single-crystal diamond - a transmission electron microscopy study, Diam. Relat. Mater. 18 (11) (nov 2009) 1353–1359.
[10] P. Olivero, G. Amato, F. Bellotti, O. Budnyk, E. Colombo, M. Jakšić, C. Manfredotti, Ž. Pastuović, F. Picollo, N. Skukan, M. Vannoni, E. Vittone, Direct fabrication of three-dimensional buried conductive channels in single crystal diamond with ion microbeam induced graphitization, Diam. Relat. Mater. 18 (5–8) (may 2009) 870–876.
[11] J.J. Hauser, J.R. Patel, Hopping conductivity in c-implanted amorphous diamond, or how to ruin a perfectly good diamond, Solid State Commun. 18 (7) (1976) 789–790.
[12] J.J. Hauser, J.R. Patel, J.W. Rodgers, Hard conducting implanted diamond layers, Appl. Phys. Lett. 30 (3) (feb 1977) 129–130.
[13] J.F. Prins, Electrical resistance of diamond implanted at liquid nitrogen temperature with carbon ions, Radiat. Eff. 76 (3) (jan 1983) 79–82.
[14] J.F. Prins, Onset of hopping conduction in carbon-ion-implanted diamond, Phys. Rev. B 31 (4) (feb 1985) 2472–2478.
[15] A. Reznik, V. Richter, R. Kalish, Kinetics of the conversion of broken diamond (sp3) bonds to graphitic (sp2) bonds, Phys. Rev. B 56 (13) (oct 1997) 7930–7934.
[16] A. Reznik, V. Richter, R. Kalish, The re-arrangement of broken bonds in damaged diamond: graphitization versus annealing back to diamond, Diam. Relat. Mater. 7 (2–5) (feb 1998) 317–321.
[17] E. Baskin, A. Reznik, D. Saada, Joan Adler, R. Kalish, Model for the defect-related electrical conductivity in ion-damaged diamond, Phys. Rev. B 64 (22) (nov 2001) 224110.
[18] S. Prawer, Ion implantation of diamond and diamond films, Diam. Relat. Mater. 4 (5–6) (may 1995) 862–872.
[19] F. Fontaine, E. Gheeraert, A. Deneuville, Conduction mechanisms in boron implanted diamond films, Diam. Relat. Mater. 5 (6–8) (may 1996) 752–756.
[20] J.F. Prins, Ballistic self-annealing during ion implantation, J. Phys. Appl. Phys. 34 (20) (oct 2001) 3003–3010.
[21] J. Zhou, B. Liao, B. Qiu, S. Huberman, K. Esfarjani, M.S. Dresselhaus, G. Chen, Ab initio optimization of phonon drag effect for lower-temperature thermoelectric energy conversion, Proc. Natl. Acad. Sci. USA 112 (48) (nov 2015) 14777–14782.
[22] N.H. Protik, B. Kozinsky, Electron-phonon drag enhancement of transport properties from a fully coupled ab initio Boltzmann formalism, Phys. Rev. B 102 (24) (dec 2020) 245202.
[23] R. Sen, N. Vast, J. Sjakste, Role of dimensionality and size in controlling the drag seebeck coefficient of doped silicon nanostructures: a fundamental understanding, Phys. Rev. B 108 (6) (aug 2023) l060301.
[24] A.I. Boukai, Y. Bunimovich, J. Tahir-Kheli, J.K. Yu, W.A. Goddard III, J.R. Heath, Silicon nanowires as efficient thermoelectric materials, Nature 451 (7175) (jan 2008) 168–171.
[25] K. Fauziah, Y. Suzuki, T. Nogita, Y. Kamakura, T. Watanabe, F. Salleh, H. Ikeda, Effect of phonon-boundary scattering on phonon-drag factor in seebeck coefficient of si wire, AIP Adv. 10 (7) (2020) jul.
[26] J. Ma, D. Gelda, K.V. Valavala, S. Sinha, Peak thermoelectric power factor of holey silicon films, J. Appl. Phys. 128 (11) (sep 2020).
[27] S. Li, A. Wang, Y. Hu, X. Gu, Z. Tong, H. Bao, Anomalous thermal transport in metallic transition-metal nitrides originated from strong electron–phonon interactions, Materials Today Physics 15 (dec 2020) 100256.
[28] G. Wang, L. Endicott, H. Chi, P. Lošťák, C. Uher, Tuning the temperature domain of phonon drag in thin films by the choice of substrate, Phys. Rev. Lett. 111 (4) (jul 2013) 046803.
[29] J.F. Prins, Ion-implanted structures and doped layers in diamond, Mater. Sci. Rep. 7 (7–8) (feb 1992) 275–364.
[30] J.F. Ziegler, M.D. Ziegler, J.P. Biersack, Srim – the stopping and range of ions in matter, Nucl. Instrum. Methods Phys. Res. Sect. B Beam Interact. Mater. Atoms 268 (11–12) (2010) 1818–1823, jun 2010.
[31] C. Uzan-Saguy, C. Cytermann, R. Brener, V. Richter, M. Shaanan, R. Kalish, Damage threshold for ion-beam induced graphitization of diamond, Appl. Phys. Lett. 67 (9) (aug 1995) 1194–1196.
[32] P. Olivero, S. Rubanov, P. Reichart, B.C. Gibson, S.T. Huntington, J.R. Rabeau, Andrew D. Greentree, J. Salzman, D. Moore, D.N. Jamieson, S. Prawer, Characterization of three-dimensional microstructures in single-crystal diamond, Diam. Relat. Mater. 15 (10) (oct 2006) 1614–1621.
[33] S. Rubanov, A. Suvorova, Ion implantation in diamond using 30kev ga+ focused ion beam, Diam. Relat. Mater. 20 (8) (aug 2011) 1160–1164.
[34] I. Motochi, S.R. Naidoo, B.A. Mathe, R. Erasmus, E. Aradi, T.E. Derry, E.J. Olivier, Surface brillouin scattering on annealed ion-implanted CVD diamond, Diam. Relat. Mater. 56 (6–12) (jun 2015).
[35] R.A. Spits, T.E. Derry, J.F. Prins, Annealing studies on ion implanted diamond, Nucl. Instrum. Methods Phys. Res. Sect. B Beam Interact. Mater. Atoms 64 (1–4) (feb 1992) 210–214.
[36] R. Kalish, A. Reznik, S. Prawer, D. Saada, J. Adler, Ion-implantation-induced defects in diamond and their annealing: Experiment and simulation, Phys. Status Solidi 174 (1) (jul 1999) 83–99.
[37] E.K. Nshingabigwi, T.E. Derry, S.R. Naidoo, J.H. Neethling, E.J. Olivier, J. H. O'Connell, C.M. Levitt, Electron microscopy profiling of ion implantation damage in diamond: dependence on fluence and annealing, Diam. Relat. Mater. 49 (1–8) (oct 2014).
[38] R. Kalish, A. Reznik, K.W. Nugent, S. Prawer, The nature of damage in ion-implanted and annealed diamond, Nucl. Instrum. Methods Phys. Res. Sect. B Beam Interact. Mater. Atoms 148 (1–4) (jan 1999) 626–633.
[39] F. Bosia, S. Calusi, L. Giuntini, S. Lagomarsino, A.L. Giudice, M. Massi, P. Olivero, F. Picollo, S. Sciortino, A. Sordini, M. Vannoni, E. Vittone, Finite element analysis of ion-implanted diamond surface swelling, Nucl. Instrum. Methods Phys. Res. Sect. B Beam Interact. Mater. Atoms 268 (19) (oct 2010) 2991–2995.
[40] F. Bosia, N. Argiolas, M. Bazzan, P. Olivero, F. Picollo, A. Sordini, M. Vannoni, E. Vittone, Modification of the structure of diamond with MeV ion implantation, Diam. Relat. Mater. 20 (5–6) (may 2011) 774–778.
[41] R.A. Khmelnitsky, V.A. Dravin, A.A. Tal, M.I. Latushko, A.A. Khomich, A. V. Khomich, A.S. Trushin, A.A. Alekseev, S.A. Terentiev, Mechanical stresses and amorphization of ion-implanted diamond, Nucl. Instrum. Methods Phys. Res. Sect. B Beam Interact. Mater. Atoms 304 (5–10) (jun 2013).
[42] F. Bosia, N. Argiolas, M. Bazzan, B.A. Fairchild, A.D. Greentree, D.W.M. Lau, P. Olivero, F. Picollo, S. Rubanov, S. Prawer, Direct measurement and modelling of internal strains in ion-implanted diamond, J. Phys. Condens. Matter 25 (38) (aug 2013) 385403.
[43] R.A. Khmelnitsky, V.A. Dravin, A.A. Tal, E.V. Zavedeev, A.A. Khomich, A. V. Khomich, A.A. Alekseev, S.A. Terentiev, Damage accumulation in diamond during ion implantation, J. Mater. Res. 30 (9) (feb 2015) 1583–1592.
[44] W.P. Leroy, C. Detavernier, R.L. Van Meirhaeghe, C. Lavoie, Thin film solid-state reactions forming carbides as contact materials for carbon-containing semiconductors, J. Appl. Phys. 101 (5) (2007).
[45] Y. Hoshino, Y. Saito, J. Nakata, Interdiffusion analysis of au/ti and au/pt/ti electrode structures grown on diamond (001) surface by rutherford backscattering spectroscopy, Jpn. J. Appl. Phys. 49 (10R) (oct 2010) 101302.
[46] S. Kono, T. Teraji, H. Kodama, K. Ichikawa, S. Ohnishi, A. Sawabe, Direct determination of the barrier height of ti-based ohmic contact on p-type diamond (001), Diam. Relat. Mater. 60 (nov 2015) 117–122.
[47] D. Bérardan, E. Alleno, C. Godart, O. Rouleau, J. Rodriguez-Carvajal, Preparation and chemical properties of the skutterudites (ce–yb)yFe4-x(co/ni)xSb12, Mater. Res. Bull. 40 (3) (mar 2005) 537–551.
[48] F. Picollo, D.G. Monticone, P. Olivero, B.A. Fairchild, S. Rubanov, S. Prawer, E. Vittone, Fabrication and electrical characterization of three-dimensional graphitic microchannels in single crystal diamond, New J. Phys. 14 (5) (may 2012) 053011.
[49] A. Valentin, M. De Feudis, O. Brinza, A. Tardieu, L. William, A. Tallaire, J. Achard, Characteristics of he ion implanted layers on single-crystal diamond, Phys. Status Solidi 215 (22) (sep 2018).
[50] D.E. Soule, Magnetic field dependence of the hall effect and magnetoresistance in graphite single crystals, Phys. Rev. 112 (3) (November 1958) 698–707.
[51] J.P. Jay-Gerin, R. Maynard, Phonon drag in graphite, J. Low Temp. Phys. 3 (4) (oct 1970) 377–392.
[52] C. Ayache, A. de Combarieu, J.P. Jay-Gerin, Observation of a new anomaly in the low-temperature thermoelectric power of graphite: interpretation by a phonon-drag effect acting on the h-point minority holes, Phys. Rev. B 21 (6) (mar 1980) 2462–2465.
[53] C. Uher, Thermopower of exfoliated graphites between 1.7 and 300 k, Phys. Rev. B 25 (6) (mar 1982) 4167–4172.

[54] Y. Hishiyama, A. Ono, Low temperature anomalies in thermoelectricity of highly oriented graphite in relation to sample quality, Carbon 23 (4) (1985) 445–448.
[55] T. Takezawa, T. Tsuzuku, A. Ono, Y. Hishiyama, Thermoelectric power of single-crystal graphite at low temperatures, Phil. Mag. 19 (159) (mar 1969) 623–628.
[56] K. Sugihara, H. Ohshima, K. Kawamura, T. Tsuzuku, Anomalous phonon drag effect in graphite, J. Phys. Soc. Jpn. 43 (5) (nov 1977) 1664–1671.